

Density of states in disordered graphene

Klaus Ziegler

Institut für Physik, Universität Augsburg, D-86135 Augsburg, Germany

Balázs Dóra*

Max-Planck-Institut für Physik komplexer Systeme, Nöthnitzer Strasse 38, 01187 Dresden, Germany

Peter Thalmeier

Max-Planck-Institut für Chemische Physik fester Stoffe, 01187 Dresden, Germany

(Received 19 December 2008; revised manuscript received 22 April 2009; published 24 June 2009)

We study two lattice models, the honeycomb lattice (HCL) and a special square lattice (SQL), both reducing to the Dirac equation in the continuum limit. In the presence of disorder (Gaussian potential disorder and random vector potential), we investigate the behavior of the density of states (DOS) numerically and analytically. While an upper bound can be derived for the DOS on the SQL at the Dirac point, which is also confirmed by numerical calculations, no such upper limit exists on the HCL in the presence of random vector potential. A careful investigation of the lowest eigenvalues indeed indicates that the DOS can possibly be divergent at the Dirac point on the HCL. In spite of sharing a common continuum limit, these lattice models exhibit different behavior.

DOI: [10.1103/PhysRevB.79.235431](https://doi.org/10.1103/PhysRevB.79.235431)

PACS number(s): 81.05.Uw, 71.10.-w, 72.15.-v

I. INTRODUCTION

Graphene, a two-dimensional (2D) sheet of carbon atoms forming a honeycomb lattice, has set the stage for studying Dirac-type quasiparticles in two-dimensional materials.^{1–3} A substantial part of the investigation has been devoted to the unusual transport properties of graphene. More recently, also local properties have been studied.^{4,5}

Many physical properties depend directly or indirectly on the density of (quantum) states (DOS) at the Fermi energy. Therefore, the DOS, especially near the Fermi level, is an interesting and important quantity to study. Local probing of graphene, such as in the recent scanning tunneling microscopy experiments,^{4,5} has also raised interest in the local DOS. Moreover, the DOS at the Dirac point (DP) also plays an important role as an indicator for spontaneous symmetry breaking, which causes long-range correlations in graphene.⁶

In pure graphene (or for pure Dirac fermions), in contrast to disordered graphene, the DOS vanishes linearly like $\rho(E) \sim |E|$ at the Dirac point $E=0$. Scattering by disorder may create new states⁷ at any energy, also at $E=0$. As a consequence, the linear behavior of the DOS at low energies is affected by disorder. On the other hand, the linear behavior of the DOS can be considered as a power law of a critical phenomenon with exponent 1. In fact, the phase transition in the 2D Ising model is directly linked to this linear behavior of the DOS of 2D Dirac fermions.⁸ A common belief is that disorder or additional interaction effects do not destroy the critical phenomenon but only modify the exponent of the corresponding power law. This possibility has also been discussed for the Dirac fermions, for instance, in the case of a random vector potential.^{9–11} Another possibility is that disorder creates a new intermediate phase between the two phases of the pure system.¹²

For weak disorder we can apply a perturbation theory with respect to a random vector potential. This approach gives a power law

$$\langle \rho(E) \rangle \sim |E|^\alpha \quad (\alpha \leq 1), \quad (1)$$

where the exponent decreases with increasing variance of the disorder distribution g as

$$\alpha \sim 1 - g/\pi. \quad (2)$$

On the other hand, there has been a long debate in the literature whether or not the exponent can have negative values for strong disorder (i.e., whether or not there is a divergent average DOS in the case of strong disorder) for the model with a single Dirac cone.^{9,11,13,14}

The case of two Dirac cones with intervalley scattering has also been discussed intensively in the literature.^{11,15–17} Intervalley scattering may affect the density of states strongly, leading to a power law with a universal exponent $\alpha=1/7$ for any strength of disorder.¹¹

The power law of the density of states has direct implications for the transport properties. The Einstein relation states that the conductivity σ and the DOS are proportional to each other,

$$\sigma \propto \rho(E)D(E),$$

where $D(E)$ is the diffusion coefficient. If $\rho(E)$ vanishes at the Dirac point $E=0$ for $\alpha>0$, the conductivity also vanishes as long as $D(E=0)$ is finite. The latter should be the case in the presence of disorder because $D(E)$ measures the amount of scattering since D is proportional to the scattering time τ . An exceptional case is a pure system, where transport is ballistic [$D(E \rightarrow 0) \rightarrow \infty$]. On the other hand, if $\rho(E)$ diverges at the Dirac point for $\alpha<0$, the conductivity also diverges unless the diffusion coefficient vanishes.

An alternative approach for the density of states is the self-consistent noncrossing (or Born) approximation.^{18–20} The perturbative result of the DOS in Eqs. (1) and (2) was confirmed for the tight-binding model on the honeycomb lattice (HCL) within the self-consistent calculation.¹⁰ However,

very close to $E=0$ an interception of the power law was found, indicating a nonzero DOS at $E=0$. Moreover, the calculation gave only positive exponents α , even for strong disorder, in contrast to the exponent suggested in Refs. 9 and 11,

$$\alpha = \frac{1 - g/\pi}{1 + g/\pi}.$$

In order to shed some light on the behavior of the average DOS near the Dirac point, we shall focus in this paper on two cases: (i) a single Dirac cone with random vector potential and (ii) the honeycomb lattice with unidirectional random bonds. By comparing these two cases we estimate the effect of intervalley scattering on the DOS.

The paper is organized as follows: after a brief introduction of the tight-binding model for graphene and the introduction of a specific square lattice (SQL) model, possessing Dirac fermionic excitations, we discuss the underlying symmetries of the models in Sec. II. Based on these considerations we derive a simple expression for the local DOS in the case of the single Dirac cone with random vector potential in Sec. II B. This allows us in Sec. II C to give an upper bound for the average local DOS. In the third part of the paper (Sec. III) we apply exact diagonalization (ED) to the specific square lattice model with random vector potential and to the tight-binding model on the honeycomb lattice with unidirectional bond disorder to study the energy levels near the Dirac point for finite systems.

II. MODELS AND SYMMETRIES

A. Honeycomb lattice

The starting point is a tight-binding model for quasiparticles on the honeycomb lattice, which is a bipartite lattice. After dividing it into sublattices A and B , the quasiparticles are pseudospin-1/2 particles with respect to the two sublattices, and the corresponding Hamiltonian has a chiral symmetry. This allows us to write

$$\mathbf{H} = \sum_{r,r'} \sum_{j,j'=1,2} H_{r,j;r',j'}^{\text{HCL}} c_{r,j}^\dagger c_{r',j'},$$

where r runs over sublattice A and j refers to sublattice A ($j=1$) and sublattice B ($j=2$). The only energy scale of this Hamiltonian is the nearest-neighbor hopping energy t . Nearest-neighbor hopping takes place only between different sublattices such that the Hamiltonian can also be written as

$$H^{\text{HCL}} = \begin{pmatrix} 0 & H_{AB} \\ H_{BA} & 0 \end{pmatrix},$$

where H_{AB} is acting from sublattice B to sublattice A . Here we have $H_{BA} = H_{AB}^T$ (superscript T is the transposition of matrix elements with respect to the lattice coordinates) since H is a symmetric matrix on the honeycomb lattice. Using $H_1 = (H_{AB} + H_{BA})/2$ and $H_2 = i(H_{AB} - H_{BA})/2$, the Hamiltonian matrix can be expressed with Pauli matrices as²¹

$$H^{\text{HCL}} = H_1 \sigma_1 + H_2 \sigma_2. \quad (3)$$

It should be noticed that H_1, H_2 are symmetric and antisymmetric matrices ($H_1^T = H_1, H_2^T = -H_2$) in real-space representation, respectively. Choosing a two-dimensional orthonormal basis with one vector parallel to a pair of nearest-neighbor sites, we can apply a Fourier transformation to get the Fourier components of H_1, H_2 as

$$h_1 = -t \sum_{j=1}^3 \cos(\mathbf{a}_j \cdot \mathbf{k}), \quad h_2 = -t \sum_{j=1}^3 \sin(\mathbf{a}_j \cdot \mathbf{k}), \quad (4)$$

with $\mathbf{a}_1 = a(-\sqrt{3}/2, 1/2)$, $\mathbf{a}_2 = a(0, -1)$, and $\mathbf{a}_3 = a(\sqrt{3}/2, 1/2)$ pointing toward nearest neighbors on the honeycomb lattice, where a is the lattice constant and t is the hopping integral. The corresponding quasiparticle dispersion $E_k = \pm \sqrt{h_1^2 + h_2^2}$ has two Dirac cones (two “valleys”) at low energies, $E_k \sim 0$.

B. Dirac Hamiltonian on a square lattice

Considering quasiparticles at low energies only, we can expand the Hamiltonian around both Dirac points. Then we get a model that describes two separate spin-1/2 Dirac spinors. Scattering by disorder can, in principle, connect these two Dirac cones (valleys). It has been discussed that this leads to the SU(2) Wess-Zumino-Witten model¹⁵ (but see also Ref. 13). On the other hand, if intercone scattering is ignored (for instance, by assuming a smooth scattering potential that is constant on the scale of a few lattice spacings), the two valleys of the model are completely isolated from each other and each valley can be studied separately. The corresponding Hamiltonian H_D is again a chiral spinor-1/2 Hamiltonian

$$H_D = D_1 \sigma_1 + D_2 \sigma_2. \quad (5)$$

D_1 and D_2 are given by $D_j = i[\delta_{\mathbf{r}, \mathbf{r}+\mathbf{a}_j} - \delta_{\mathbf{r}, \mathbf{r}-\mathbf{a}_j}]$, where \mathbf{a}_j are elementary lattice vectors. These matrices are now antisymmetric spatial matrices [$D_j^T = -D_j$ ($j=1,2$)] with imaginary matrix elements and the σ 's denote the sublattice degree of freedom. In contrast to the symmetric tight-binding Hamiltonian on the honeycomb lattice H^{HCL} , it breaks the time-reversal invariance because it is not symmetric: $H_D^T = H_D^* = \sigma_2 H_D \sigma_2$. (The transposition acts here on the lattice coordinates as well as on the Pauli matrices.) The Fourier components of D_1, D_2 are given by

$$d_1 = -2t \sin(k_x a), \quad d_2 = -2t \sin(k_y a). \quad (6)$$

From this, the energy spectrum follows as $E_{\pm} = \pm \sqrt{d_1^2 + d_2^2}$ and the position of the Dirac point, determined from $E_{\pm} = 0$, is given by $(k_x a, k_y a) = (n\pi, m\pi)$ with n and m integers. Altogether, there are four independent Dirac points now located at $(k_x a, k_y a) = (0,0), (0,\pi), (\pi,0)$, and (π,π) . Since these Dirac points are far apart in Fourier space, their contribution to the density of states can be separated. Moreover, we assume that D_j are lattice hopping matrix elements with nearest-neighbor elements on a square lattice whose continuum limit is the j component of the 2D gradient ∇_j . This fictitious square lattice is sketched in Fig. 1 with sublattice-dependent hopping amplitudes. Thus, the Hamiltonian H_D

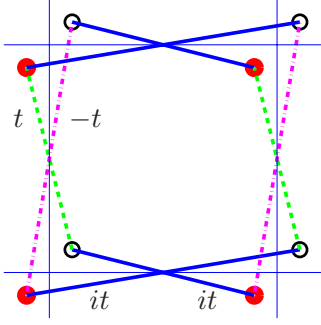


FIG. 1. (Color online) The square lattice whose continuum limit is the Dirac Hamiltonian is visualized. Filled red and empty black circles denote the two sublattices and thick/thin lines denote the hopping/lattice. The hopping matrix elements are indicated. Note the sublattice dependent hopping amplitudes.

describes lattice Dirac fermions. The connection with the tight-binding Hamiltonian H^{HCL} is only through the fact that these Hamiltonians share the same low-energy properties near their Dirac points $E_k \sim 0$. The appearance of new Dirac points (related to the fermion doubling problem²²) is not a problem here because it only multiplies the density of states with a factor 2.

Disorder can appear in H_D in form of a random scalar potential, a random mass, or a random vector potential.⁹ Only the latter preserves the continuous chiral symmetry. It is believed that this type of disorder is related to ripples in the graphene sheet.^{23,24} In the following, disorder due to ripples will be considered. This can be represented by a random vector potential $(V_{1,r}, V_{2,r})$ as

$$H = (D_1 + V_1)\sigma_1 + (D_2 + V_2)\sigma_2. \quad (7)$$

This Hamiltonian has three essential symmetry properties: it is Hermitian (i.e., $H^\dagger = H$), it satisfies the following relations,

$$\sigma_3 H \sigma_3 = -H, \quad (8)$$

and with the staggered diagonal matrix D ,

$$D_{rj,r'j'} = (-1)^{r_1+r_2} \delta_{r,r'} \delta_{j,j'},$$

we get (cf. Appendix A)

$$\sigma_1 D H^T D \sigma_1 = H. \quad (9)$$

The fact that H is Hermitian implies for the Green's function $G(i\epsilon) = (i\epsilon + H)^{-1}$ the relation

$$G^\dagger(i\epsilon) = G(-i\epsilon). \quad (10)$$

Moreover, Eq. (8) implies

$$\sigma_3 G(i\epsilon) \sigma_3 = -G(-i\epsilon), \quad (11)$$

and Eq. (9) implies

$$\sigma_1 D G(i\epsilon)^T D \sigma_1 = G(i\epsilon). \quad (12)$$

The spatial diagonal elements of the Green's function $G_{rr}(i\epsilon)$ can be expressed in terms of Pauli matrices as

$$G_{rr}(i\epsilon) = g_0(i\epsilon)\sigma_0 + g_1(i\epsilon)\sigma_1 + g_2(i\epsilon)\sigma_2 + g_3(i\epsilon)\sigma_3. \quad (13)$$

The three relations in Eqs. (10)–(12) provide the following relations between the coefficients of the Pauli matrices:

$$g_0^*(i\epsilon) = g_0(-i\epsilon) = -g_0(i\epsilon),$$

$$g_1^*(i\epsilon) = g_1(-i\epsilon) = g_1(i\epsilon),$$

$$g_2^*(i\epsilon) = g_2(-i\epsilon) = g_2(i\epsilon),$$

$$g_3(i\epsilon) = 0.$$

Note that this is a clear consequence of Eq. (12), which holds true only on the square lattice. Thus, g_0 is purely imaginary, whereas g_1 and g_2 are real and g_3 vanishes,

$$G_{rr}(i\epsilon) = g_0(i\epsilon)\sigma_0 + g_1(i\epsilon)\sigma_1 + g_2(i\epsilon)\sigma_2. \quad (14)$$

C. Local density of states of Dirac fermions

The Green's function $G = (i\epsilon + H_D)^{-1}$ allows us to write for the local DOS for a fixed random disorder configuration

$$\rho_r = -\frac{1}{2\pi} \text{Im Tr}_2(G_{rr}), \quad (15)$$

where $\epsilon > 0$ is implicitly sent to zero and the trace Tr_2 is taken with respect to the Pauli matrices. As a function of the random vector potential at site r ($V_{1,r}, V_{2,r}$), the local DOS ρ_r of the Green's function in Eq. (14) has a Lorentzian form [cf. Eq. (B1) in Appendix B]

$$\rho_r = \frac{1}{\pi} \frac{(X_0 + \epsilon)}{(X_0 + \epsilon)^2 + (X_1 + V_{1,r})^2 + (X_2 + V_{2,r})^2} \quad (16)$$

with some real variables X_1, X_2 and a positive real variable $\epsilon + X_0$, where the latter is proportional to ϵ . They depend on $V_{1,r}, V_{2,r}$ for $r' \neq r$ but not on $V_{1,r}, V_{2,r}$. This expression can also be used to determine the DOS away from the Dirac point at energy $E \neq 0$ by replacing $\epsilon \rightarrow \epsilon - iE$,

$$\rho_r(E) = \frac{1}{\pi} \text{Re} \left[\frac{(X_0 + \epsilon - iE)}{(X_0 + \epsilon - iE)^2 + (X_1 + V_{1,r})^2 + (X_2 + V_{2,r})^2} \right]. \quad (17)$$

It should be noticed that this form of the local DOS is very special for the Green's function in Eq. (14). For instance, we would not get a Lorentzian in the case of a random scalar potential.

Expression (17) enables us to evaluate the local DOS $\rho_r(E)$ for the extreme case of an impurity at site r . According to Eq. (B2) the parameters X_j ($j=0, 1, 2, 3$) of the system without disorder are

$$X_0 = -\epsilon + iE - i/g_0, \quad X_1 = X_2 = X_3 = 0,$$

where

$$g_0 = - \int \frac{i\epsilon + E}{(\epsilon - iE)^2 + k^2} \frac{d^2k}{(2\pi)^2}. \quad (18)$$

We can also study a local scalar potential E_r by adding $-iE_r$ to X_0 in Eq. (17). Then the local DOS reads for the local random vector potential and for the local random scalar potential, respectively,

$$\rho_r(E, V_{1,r}) = \frac{1}{\pi} \text{Re} \left[\frac{ig_0}{1 - g_0^2 V_{1,r}^2} \right],$$

$$\rho_r(E, E_r) = \frac{1}{\pi} \text{Re} \left[\frac{ig_0}{1 - g_0 E_r} \right].$$

The contribution of the two local potentials is quite different: while $\rho_r(E, V_{1,r})$ is always symmetric in E as a consequence of $g_0(E)^* = -g_0(-E)$,

$$2 \text{Re} \left[\frac{ig_0}{1 - g_0^2 V_{1,r}^2} \right] = \frac{ig_0(E)}{1 - g_0(E)^2 V_{1,r}^2} + \frac{ig_0(-E)}{1 - g_0(-E)^2 V_{1,r}^2},$$

the local DOS $\rho_r(E, E_r)$ is not symmetric in general. This allows us to distinguish between the two types of local disorder by measuring the shape of the local DOS.

A direct evaluation of the variables $X_j (j=0, 1, 2, 3)$ is difficult in the general case, where we have a random vector potential at all sites. However, for finite and sufficiently small systems an exact diagonalization is possible. Moreover, we can derive an upper bound for the average local DOS. This will be discussed in Sec. II D.

D. Upper bound for the DOS of Dirac fermions

Now we perform the integration with respect to (V_1, V_2) for all sites to evaluate the average local DOS. For simplicity, we consider only the Dirac point $E=0$ here,

$$\langle \rho_r \rangle = \int \rho_r \prod_{r'} P(V_{1,r'}) dV_{1,r'} P(V_{2,r'}) dV_{2,r'}. \quad (19)$$

First, we perform the integration with respect to $V_{1,r}$ using the expression of ρ_r in Eq. (16),

$$\int \rho_r P(V_{1,r}) dV_{1,r} = \frac{1}{\pi} \int \frac{(X_0 + \epsilon)}{(X_0 + \epsilon)^2 + (X_1 + V_{1,r})^2 + (X_2 + V_{2,r})^2} P(V_{1,r}) dV_{1,r}.$$

An upper bound for this integral is obtained from pulling out the maximum of the distribution density $P(V_{1,r})$ which we call P_m : $P(V_{1,r}) \leq P_m$. This gives

$$\int \rho_r P(V_{1,r}) dV_{1,r} \leq \frac{P_m}{\pi} \int \frac{(X_0 + \epsilon)}{(X_0 + \epsilon)^2 + (X_1 + V_{1,r})^2 + (X_2 + V_{2,r})^2} dV_{1,r},$$

and after integrating over the Lorentzian function, which gives π , the right-hand side becomes P_m ,

$$\int \rho_r P(V_{1,r}) dV_{1,r} \leq P_m.$$

Going back to the expression (19), we obtain

$$\langle \rho_r \rangle \leq P_m \int P(V_{2,r}) dV_{2,r} \int \prod_{r' \neq r} P(V_{1,r'}) dV_{1,r'} P(V_{2,r'}) dV_{2,r'} = P_m.$$

In other words, the averaged local DOS at the Dirac point $E=0$ has an upper bound,

$$\langle \rho_r \rangle = \frac{1}{2\pi} \text{Tr}_2(\langle \text{Im } G_{rr} \rangle) \leq \max_{-\infty < V < \infty} P(V). \quad (20)$$

This means that for any smooth bounded distribution of $V_{1,r}$ (e.g., for a Gaussian) the corresponding average local DOS ρ_r is finite. For discrete distributions, such as a binary alloy, the upper bound is infinite though.

III. EXACT DIAGONALIZATION

For a better understanding of the details of the DOS, we employ an exact diagonalization study on small clusters for both models, Hamiltonian (3) on the original HCL and Hamiltonian (7) on the effective SQL. Although both models reduce to the same continuum limit of Dirac fermions with random vector potential, they possess distinct structures in the DOS, as we will discuss below. We use Gaussian disorder with standard deviation V (i.e., V^2 is the variance).

Density of states by ED. Determining the DOS of the infinite system by studying a finite system is a difficult task since any finite system possesses distinct energy levels, resulting in separate Dirac delta peaks in the DOS at the quasiparticle energies. The DOS becomes continuous only in the thermodynamic limit. In order to avoid this problem, we choose an indirect approach to evaluate the DOS by counting the number of eigenvalues in a narrow frequency range around a given energy E . Strictly speaking, this leads to the number of states around E but if the DOS is a smooth function, this provides us with a sensible definition. We obtain the DOS shown in Fig. 2 on a 100×100 HCL cluster with periodic boundary conditions for unidirectional bond and potential disorder using a $t/500$ wide energy windows, where t is the uniform hopping amplitude. For comparison, we also show the result of the self-consistent noncrossing approximation (SCNCA) on the HCL.¹⁰ As is seen, the agreement is surprisingly good for weak disorder except for the case of bond disorder in a very close vicinity of the Dirac point. There, for $V_1 \lesssim 0.6t$, the residual DOS remains zero, which is in contrast to the finite, although exponentially small, residual value for the case of potential disorder, described correctly by the SCNCA. A narrow peak appears at the DP for bond disorder if $V_1 \gtrsim 0.6t$. Whether this peak remains finite or diverges cannot be decided within this calculation of the DOS. It should be mentioned that the DOS on a SQL is qualitatively similar to the potential disorder case on a HCL for strong disorder. In particular, it never diverges at the DP. The anomalous behavior close to the DP is obvious in per-

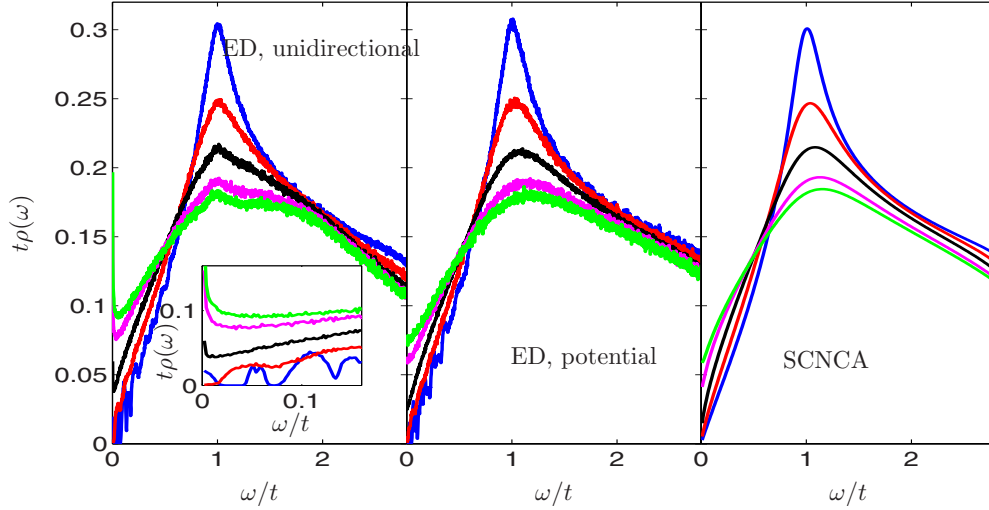


FIG. 2. (Color online) The DOS is shown as obtained by exact diagonalization on 100×100 honeycomb clusters with Gaussian unidirectional bond disorder (left panel), potential disorder (middle panel) after 1000 averages for $V_1/t = 0.3$ (blue), 0.5 (red), 0.7 (black), 0.9 (magenta), and 1 (green) from top to bottom at $\omega = t$. The right panel shows the corresponding self-consistent noncrossing approximation for the same parameters for the HCL. The inset shows the narrow peak at the DP for the unidirectional case. The SCNCA leads to the same result for pure unidirectional bond or potential disorder. Note the nice agreement between the numerical and analytical results for weak disorder.

turbation theory as well,¹⁰ where a dynamically generated low-energy scale, similar to the Kondo scale, separates the high- and low-energy regions in the DOS.

Eigenvalues. The investigation of the lowest eigenvalues in the case of unidirectional bond disorder, determining the residual DOS, may reveal some structures which are responsible for the aforementioned behavior of the DOS near the DP. Therefore, we take a single-disorder realization of H_{dis} , chosen randomly according to a Gaussian distribution. Then we diagonalize $H_{\text{HCL}} + V_1 H_{\text{dis}}$ using the Lanczos algorithm and retain the 200 eigenvalues closest to the DP (symmetric

to the DP). This procedure is repeated for different values of V_1 . The result is shown in Figs. 3 and 4 as a function of the disorder strength for a 1000×1000 cluster on the HCL and a 708×708 cluster on the SQL, having almost exactly the same number of states. This reveals three different regimes. (i) For weak disorder, the distribution of the eigenvalues is rather dilute and is not influenced significantly by disorder. This can explain the zero residual DOS in this case, where a slight rearrangement of the eigenvalues changes only the slope of the vanishing DOS. (ii) Around $V_1 \sim 0.7t$, the pattern changes drastically for the HCL, where the spectrum be-

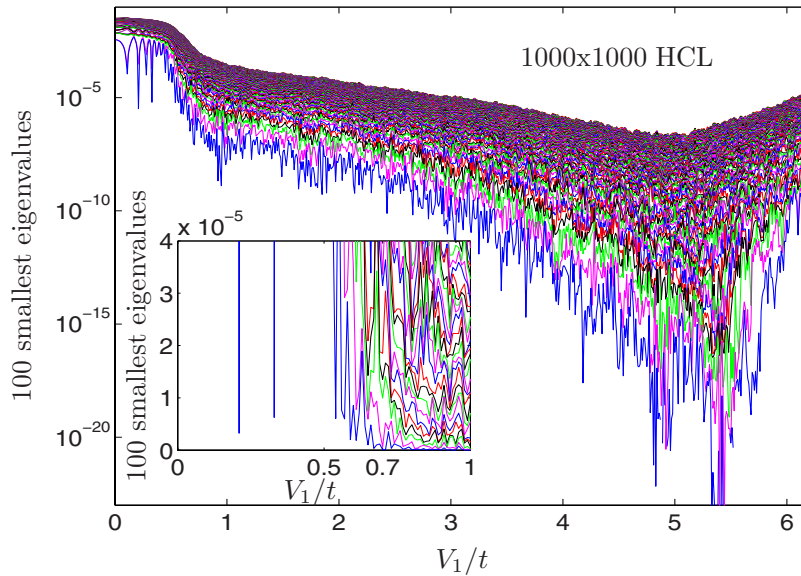


FIG. 3. (Color online) The evolution of the lowest 100 eigenvalues above the DP is shown for a 1000×1000 HCL cluster with a given Gaussian disorder configuration on a semilogarithmic scale by changing the strength of the disorder. The inset enlarges the low-energy structures and the transition from vanishing to diverging behavior. For $V_1 > 0.7T$, the eigenvalues start to approach zero rapidly, as is obvious from the semilogarithmic scale. Their increasing behavior for $V_1 > 5$ is due to finite-size effects. The statistics of the eigenvalues at $V_1 = 3t$ is depicted in Fig. 5.

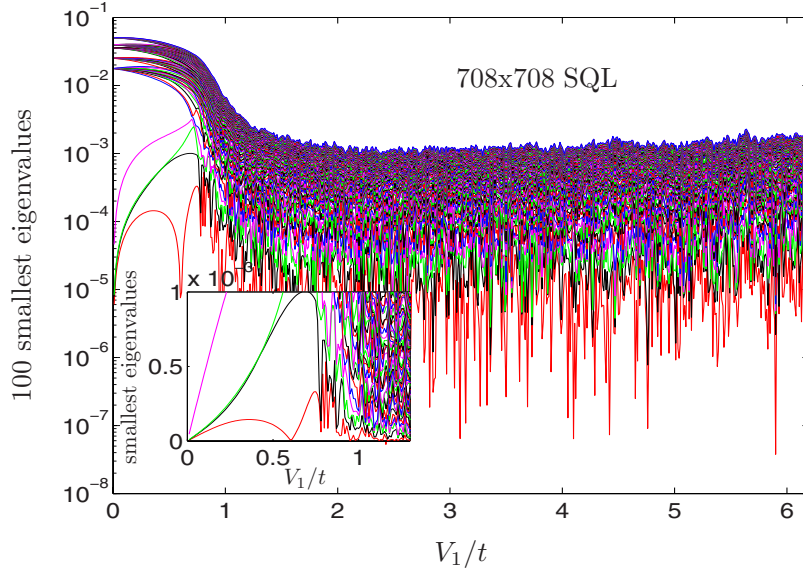


FIG. 4. (Color online) The evolution of the lowest 100 eigenvalues above the DP is shown for a 708×708 SQL cluster with a given Gaussian disorder configuration on a semilogarithmic scale by changing the strength of the disorder. The inset enlarges the low-energy structures and the transition from vanishing to diverging behavior. As opposed the HCL, the structure of the eigenvalues hardly changes for $V_1 > t$. Their distribution is shown in Fig. 5.

comes very dense close to zero energy. It keeps on decreasing monotonically down to zero energy. This behavior is responsible for the peak and a possible divergence of the DOS. (iii) For strong disorder ($V_1/t \sim 5$), the eigenvalues depart from the DP again. This crossover is related to finite-size effects since the characteristic disorder value shifts markedly to higher values with increasing system size.

This is different for the SQL. At low values of V_1 , the DOS behaves similarly for the HCL as well as for the SQL, where the DOS goes down in a power-law fashion, with decreasing exponent, but retains a finite value at the DP. For $V_1 > t$, however, the eigenvalue pattern is strongly affected only on the HCL by the explicit value of the disorder. A direct study of the DOS reveals no peak around the DP for the SQL but a finite residual value. This reflects the upper bound which was derived in Sec. II C. We mention that the isotropic bond disorder produces qualitatively similar results to the unidirectional bond disorder case on the HCL, with possibly diverging DOS at the Dirac point.

In order to obtain the DOS, we employ another approach for evaluating this quantity at the DP, which was introduced in Ref. 25: we determine the number of states $N(E)$ in a given energy interval E around the Dirac point and define the DOS as $\lim_{E \rightarrow 0} N(E)/E$. As is seen in Fig. 6, the resulting DOS for $V_1 \geq 0.7t$ shows an upturn with decreasing energy for bond disorder, which may be indicative for a diverging nature of the DOS. The DOS for $V_1 = 0.5t$ still goes to zero but the 0.7 data increases monotonically with decreasing energy. This supports the picture, that the residual DOS is indeed zero for $V \leq 0.6, \dots, 0.7t$ and changes to a diverging behavior afterward. The results for $V = 0.3t$ are probably strongly affected by finite-size effects. By fitting the resulting curves with a power law, we determine the exponent (α) which is characterizing the DOS close to the DP (cf. Fig. 7). From α the dynamical exponent z follows as $z = 2/(1 + \alpha)$.

According to Ref. 25, the latter changes its behavior at $z = 3$, which is reached here at $V_1/t \sim 2.5$, and it increases linearly with V_1 . For comparison, the case of potential disorder is plotted as well in Fig. 8, where the DOS tends smoothly to a constant value at $E = 0$. The SQL with V_1 disorder exhibits qualitatively similar behavior to the potential disorder case on the HCL.

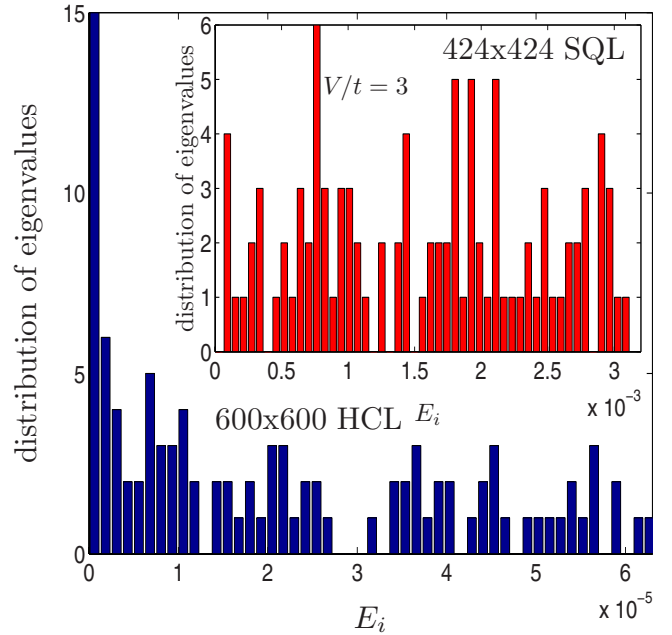


FIG. 5. (Color online) A typical distribution of the lowest eigenvalues is shown for $V/t = 3$ for both the HCL and the SQL. In the former case, the eigenvalues precipitate to zero very fast, resulting in a sharp peak around zero energy. As opposed to this, the distribution for the SQL is more uniform, yielding a nondiverging constant DOS.

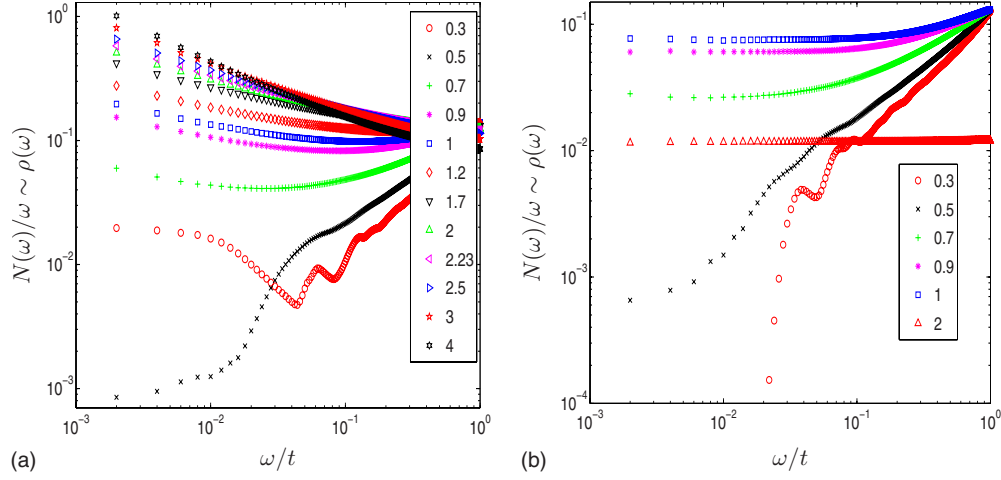


FIG. 6. (Color online) The number of states divided by energy $[\sim \rho(\omega)]$ is plotted as obtained by exact diagonalization on 100×100 honeycomb clusters with Gaussian unidirectional bond disorder (left panel) and potential disorder (right panel) after 1000 averages for several values of the disorder. The upturn with decreasing energy for bond disorder is indicative to the diverging DOS at $E=0$ for $V/t \gtrsim 0.6$.

Finite DOS on the SQL. Now we turn our attention to the square lattice model in Eq. (5). For the pure system, there is no difference between the HCL and the SQL for the DOS near the DP since excitations close to half filling are Dirac fermions in both cases. Thus, the DOS increases linearly with energy. It also exhibits a weak logarithmic singularity at the saddle point of the spectrum and falls off monotonically with increasing energy toward the band edge, as is seen in the inset of Fig. 9. The V_1 disorder in Eq. (7) on the lattice model plays the role of a random vector potential, which is perpendicular to the (pseudo)spin-quantization axis σ_3 . In the presence of V_1 disorder the DOS on the SQL is different from that of the HCL with unidirectional bond disorder: no peak develops at zero energy for strong disorder, and the DOS terminates at a finite value with vanishing slope, similarly to potential disorder in the HCL. Using an energy window of $t/500$ as for the HCL, we can evaluate the DOS as described above. The residual values are plotted in Fig. 9 and compared with the upper bound. As is seen, the upper bound becomes very sharp for strong disorder in this case and does not seem to apply to the HCL with a possibly diverging DOS.

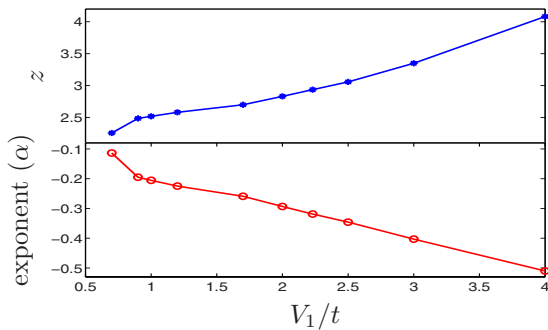


FIG. 7. (Color online) The exponents of the DOS $[\rho(\omega) \sim \omega^\alpha]$ and the dynamical exponent $z=2/(1+\alpha)$ are plotted for the HCL for strong disorder. Note the horizontal axis, which is the standard deviation and not the variance.

IV. CONCLUSIONS

We have evaluated the eigenvalues and the average DOS for the tight-binding model on the honeycomb lattice with random unidirectional bonds and for Dirac fermions on the square lattice with random vector potential. Both models have the same continuum limit, namely, Dirac fermions with a random vector potential. The model on the square lattice can be considered as a network approximation of the honeycomb lattice,²⁶ where the shortest scale of the network model is the mean-free path of disorder scattering. The latter can be much larger than the interatomic distance a of the tight-binding model with Hamiltonian H^{HCL} . This implies that microscopic properties are ignored except for those with very low energies. However, in their lattice form the density of states of our models differ substantially near the Dirac point: in the model on the honeycomb lattice the average DOS has

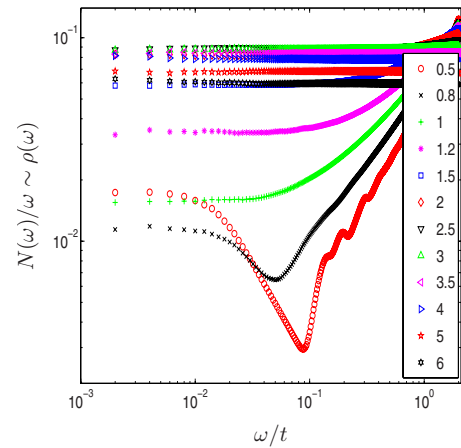


FIG. 8. (Color online) The number of states divided by energy $[\sim \rho(\omega)]$ is plotted as obtained by exact diagonalization on 90×90 square lattice after 1000 averages for several values of the V_1 disorder. It resembles closely to the potential disorder case of the HCL.

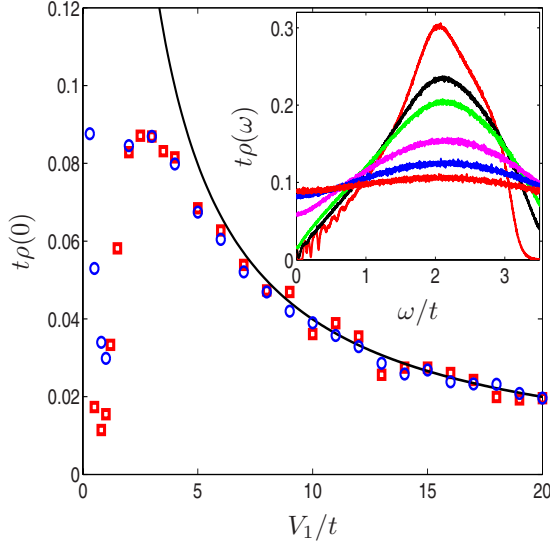


FIG. 9. (Color online) The residual DOS of the square lattice [Eq. (7)] is plotted, obtained on 90×90 and 30×30 clusters with Gaussian V_1 disorder (red squares and blue circles) after 10^3 and 10^4 averages, respectively. The black straight line is the upper bound, $\rho(0) < 1/\sqrt{2\pi}V_1$. Note that it does not involve any fitting parameter and becomes very sharp for strong disorder. Larger systems show similar behavior. Inset: the DOS of a 90×90 SQL is shown after 1000 averages for $V_1/t = 0.5, 0.8, 1, 1.5, 2$, and 2.5 with decreasing peak position at $\omega = 2t$.

a sharp peak which is not present in the model on the square lattice. Although it is not entirely clear, whether or not this peak survives the limit of the infinite system, its existence on the finite cluster is remarkable. The evolution of the eigenvalues close to the Dirac point in large systems supports the idea of a diverging peak in the DOS. We have also checked numerically that isotropic bond disorder produces similar behavior.

We have studied the effect of potential disorder on the honeycomb lattice as well, which exhibits qualitatively similar behavior to the square lattice with random vector potential but differs from the case of random unidirectional bond on the honeycomb lattice at low energies in the DOS: the residual DOS always takes a finite although exponentially small value.^{27,28} These results can surprisingly well be reproduced for weak and moderately strong disorders using the self-consistent noncrossing approximation, except for the low-energy structures in the case of bond disorder.

Using the mapping of the model on the HCL to the SU(2) gauge-field theory,^{11,15–17} the presumably exact power law of the latter $\rho \sim |E|^{1/7}$ in Ref. 11 represents a puzzle for the approximation of disordered lattice models by their corresponding continuum counterparts. The same is true for the model on the square lattice, where the DOS at the Dirac point has an upper bound according to Eq. (20). In contrast, for the continuum limit several groups found a power law with the exponent^{9,11}

$$\alpha = \frac{1 - g/\pi}{1 + g/\pi},$$

which is negative for sufficiently strong disorder. This poses severe questions on the applicability of universality idea. Al-

though both lattice models reduce to the same continuum limit and are expected to behave in a similar manner, as dictated by the common continuum limit, this is apparently not the case here. We have also checked the case of uniform disorder distribution and found similar results. The above results were found to be robust with respect to variations in system size, boundary conditions, and disorder distribution.

ACKNOWLEDGMENTS

We acknowledge useful discussions with O. Vafeek, I. Herbut, and R. Moessner. We are grateful to B. Schmidt and A. Ványolos for technical assistance. This work was supported by the Hungarian Scientific Research Fund under Grant No. OTKA K72613, by a grant from the Deutsche Forschungsgemeinschaft, and in part by the Swedish Research Council.

APPENDIX A: DISCRETE SYMMETRY

From $D_j^T = -D_j$ and $\sigma_1^T = \sigma_1$, $\sigma_2^T = -\sigma_2$ follows

$$H^T = (-D_1 + V_1)\sigma_1 - (-D_2 + V_2)\sigma_2.$$

Next, the staggered potential D changes the sign of nearest-neighbor matrix elements,

$$DH^TD = (D_1 + V_1)\sigma_1 - (D_2 + V_2)\sigma_2,$$

and σ_1 anticommutes with σ_2 ,

$$\sigma_1 DH^TD \sigma_1 = (D_1 + V_1)\sigma_1 + (D_2 + V_2)\sigma_2 = H.$$

APPENDIX B: MATRIX ELEMENTS OF THE GREEN'S FUNCTION

The spatial diagonal matrix elements of the Green's function have been given in Eq. (14). Another way to write G_{rr} is by projecting it with P_r onto the site r . This gives the matrix identity²⁹

$$G_{rr} \equiv P_r G P_r = [i\epsilon + V_r \sigma_1 + V'_r \sigma_2 - P_r H (1 - P_r) G_{1-P_r} (1 - P_r) H P_r]_{P_r}^{-1},$$

where G_{1-P_r} is the Green's function $G(i\epsilon) = (i\epsilon + H)^{-1}$ on the Hilbert space where the site r has been removed. The 2×2 matrix $P_r H (1 - P_r) G_{1-P_r} (1 - P_r) H P_r$ does not depend on the random variables V_r and V'_r . Its general form is

$$P_r H (1 - P_r) G_{1-P_r} (1 - P_r) H P_r = - \begin{bmatrix} iX_0 + X_3 & -iX_2 + X_1 \\ iX_2 + X_1 & iX_0 - X_3 \end{bmatrix}.$$

Here, the X_n 's do not depend on V_r and V'_r by construction, ensured by the projection operators. Therefore, G_{rr} reads

$$G_{rr} = \begin{bmatrix} i\epsilon + iX_0 + X_3 & -iX_2 + X_1 + V_r - iV'_r \\ iX_2 + X_1 + V_r + iV'_r & i\epsilon + iX_0 - X_3 \end{bmatrix}^{-1} \\ = - \frac{1}{(\epsilon + X_0)^2 + X_3^2 + (X_1 + V_r)^2 + (X_2 + V'_r)^2} \\ \times \begin{bmatrix} i\epsilon + iX_0 - X_3 & iX_2 + X_1 + V_r + iV'_r \\ -iX_2 + X_1 + V_r - iV'_r & i\epsilon + iX_0 + X_3 \end{bmatrix}. \quad (\text{B1})$$

This result can be compared with Eq. (14) to obtain the relations

$$X_1 = -V_r + \frac{g_1}{-g_0^2 + g_1^2 + g_2^2}, \quad iX_0 = -i\epsilon - \frac{g_0}{-g_0^2 + g_1^2 + g_2^2},$$

$$X_2 = -V'_r + \frac{g_2}{-g_0^2 + g_1^2 + g_2^2}, \quad (B2)$$

and

$$X_3 = 0.$$

All three matrix elements X_0, X_1, X_2 are real since g_0 is purely imaginary and g_1 as well as g_2 are real.

Finally, we can use the block-matrix inverse to show that g_0 is proportional to $-i\epsilon$ with a positive proportionality fac-

tor. Choosing the diagonal blocks with respect to the sublattice (or spinor) index j , we obtain

$$G_{11} = [i\epsilon - (D_1 + V_1 - iD_2 - iV_2)(D_1 + V_1 + iD_2 + iV_2)/i\epsilon]^{-1}$$

$$= -i\epsilon[\epsilon^2 + (D_1 + V_1 - iD_2 - iV_2)(D_1 + V_1 + iD_2 + iV_2)]^{-1}$$

$$= -i\epsilon[\epsilon^2 + (D_1 + V_1 - iD_2 - iV_2)(D_1 + V_1 - iD_2 - iV_2)^\dagger]^{-1}$$

and

$$G_{22} = [i\epsilon - (D_1 + V_1 + iD_2 + iV_2)(D_1 + V_1 - iD_2 - iV_2)/i\epsilon]^{-1}$$

$$= -i\epsilon[\epsilon^2 + (D_1 + V_1 + iD_2 + iV_2)(D_1 + V_1 - iD_2 - iV_2)]^{-1}$$

$$= -i\epsilon[\epsilon^2 + (D_1 + V_1 - iD_2 - iV_2)^\dagger \times (D_1 + V_1 - iD_2 - iV_2)]^{-1}.$$

Thus $iX_0 + i\epsilon = ci\epsilon$ with $c > 0$.

*dora@pks.mpg.de

- ¹K. S. Novoselov, A. K. Geim, S. V. Morozov, D. Jiang, M. I. Katsnelson, I. V. Grigorieva, S. V. Dubonos, and A. A. Firsov, *Nature* (London) **438**, 197 (2005).
- ²Y. Zhang, Y.-W. Tan, H. L. Stormer, and P. Kim, *Nature* (London) **438**, 201 (2005).
- ³A. K. Geim and K. S. Novoselov, *Nature Mater.* **6**, 183 (2007).
- ⁴J. Martin, N. Akerman, G. Ulbricht, T. Lohmann, J. H. Smet, K. von Klitzing, and A. Yacoby, *Nat. Phys.* **4**, 144 (2008).
- ⁵Y. Zhang, Victor W. Brar, Feng Wang, Caglar Girit, Yossi Yaron, Melissa Panlasigui, Alex Zettl, and Michael F. Crommie, *Nat. Phys.* **4**, 627 (2008).
- ⁶K. Ziegler, *Phys. Rev. B* **78**, 125401 (2008).
- ⁷Vitor M. Pereira, F. Guinea, J. M. B. Lopes dos Santos, N. M. R. Peres, and A. H. Castro Neto, *Phys. Rev. Lett.* **96**, 036801 (2006).
- ⁸T. D. Schultz, D. C. Mattis, and E. H. Lieb, *Rev. Mod. Phys.* **36**, 856 (1964).
- ⁹A. W. W. Ludwig, Matthew P. A. Fisher, R. Shankar, and G. Grinstein, *Phys. Rev. B* **50**, 7526 (1994).
- ¹⁰B. Dóra, K. Ziegler, and P. Thalmeier, *Phys. Rev. B* **77**, 115422 (2008).
- ¹¹A. A. Nersisyan, A. M. Tsvelik, and F. Wenger, *Phys. Rev. Lett.* **72**, 2628 (1994).
- ¹²R. B. Griffiths, *Phys. Rev. Lett.* **23**, 17 (1969).
- ¹³A. Altland, B. D. Simons, and M. R. Zirnbauer, *Phys. Rep.* **359**, 283 (2002).
- ¹⁴F. Guinea, B. Horovitz, and P. Le Doussal, *Phys. Rev. B* **77**, 205421 (2008).
- ¹⁵M. J. Bhaseen, J.-S. Caux, I. I. Kogan, and A. M. Tsvelik, *Nucl. Phys. B* **618**, 465 (2001).
- ¹⁶M. S. Foster and I. L. Aleiner, *Phys. Rev. B* **77**, 195413 (2008).
- ¹⁷J.-S. Caux, N. Taniguchi, and A. M. Tsvelik, *Phys. Rev. Lett.* **80**, 1276 (1998).
- ¹⁸H. Suzuura and T. Ando, *Phys. Rev. Lett.* **89**, 266603 (2002).
- ¹⁹N. M. R. Peres, F. Guinea, and A. H. Castro Neto, *Phys. Rev. B* **73**, 125411 (2006).
- ²⁰M. Koshino and T. Ando, *Phys. Rev. B* **73**, 245403 (2006).
- ²¹K. Ziegler, *Phys. Rev. Lett.* **100**, 166801 (2008).
- ²²H. B. Nielsen and N. Ninomiya, *Nucl. Phys. B* **185**, 20 (1981); J. B. Kogut, *Rev. Mod. Phys.* **55**, 775 (1983).
- ²³S. V. Morozov, K. S. Novoselov, M. I. Katsnelson, F. Schedin, L. A. Ponomarenko, D. Jiang, and A. K. Geim, *Phys. Rev. Lett.* **97**, 016801 (2006).
- ²⁴A. H. Castro Neto, F. Guinea, N. M. R. Peres, K. S. Novoselov, and A. K. Geim, *Rev. Mod. Phys.* **81**, 109 (2009).
- ²⁵O. Motrunich, K. Damle, and D. A. Huse, *Phys. Rev. B* **65**, 064206 (2002).
- ²⁶I. Snyman, J. Tworzydło, and C. W. J. Beenakker, *Phys. Rev. B* **78**, 045118 (2008).
- ²⁷S. Wu, L. Jing, Q. Li, Q. W. Shi, J. Chen, H. Su, X. Wang, and J. Yang, *Phys. Rev. B* **77**, 195411 (2008).
- ²⁸Ben Yu-Kuang Hu, E. H. Hwang, and S. Das Sarma, *Phys. Rev. B* **78**, 165411 (2008).
- ²⁹<http://www.cs.nthu.edu.tw/jang/book/addenda/matinv/matinv/>